1992AJ....104..241A

THE ORBIT OF α EQUULEI MEASURED WITH LONG-BASELINE OPTICAL INTERFEROMETRY: COMPONENT MASSES, SPECTRAL TYPES, AND EVOLUTIONARY STATE

J. T. ARMSTRONG,[1] D. MOZURKEWICH,[2] M. VIVEKANAND,[1,3] R. S. SIMON,[2] C. S. DENISON,[4] AND K. J. JOHNSTON[2]

NRL/USNO Optical Interferometer Project,[5] U. S. Naval Observatory, 34th St. & Massachusetts Ave. NW, Washington, DC 20392

X.-P. PAN

Astronomy Department, California Institute of Technology, Pasadena, California 91125

M. SHAO AND M. M. COLAVITA

Jet Propulsion Laboratory, Pasadena, California 91109

Received 18 November 1991; revised 13 February 1992

ABSTRACT

We present the orbit of the double-lined spectroscopic binary α Equulei, and masses and absolute magnitudes for its components, from observations with the Mark III Optical Interferometer.[5] Our orbit with the spectroscopic results of Rosvick & Scarfe [MNRAS, 252, 68 (1991)] imply masses and 1σ uncertainties of $2.13 \pm 0.29\ \mathcal{M}_\odot$ for the G primary and $1.86 \pm 0.21\ \mathcal{M}_\odot$ for the A secondary. The magnitude differences that we measure at the four observed wavelengths are consistent with a G5 III primary and an A5 V secondary, with an uncertainty of about 1.5 subtypes. We compare the masses, magnitude differences, and absolute magnitudes determined here with the evolutionary models of VandenBerg [ApJS, 58, 711 (1985)] and infer that the metallicity $Z = Z_\odot$. The masses of the G and A components from the orbital fit agree with the evolutionary masses (2.36–2.75 $\mathcal{M}_\odot$ and 2.01–2.14 $\mathcal{M}_\odot$, respectively) that fit their derived colors and absolute magnitudes. The best-fit age from the evolutionary model is 0.5–0.65 Gyr. The parallax of the system obtained from combining the spectroscopic and interferometric data, for which the term "orbital parallax" has been suggested, is given by $\pi_{\rm orb} = 0\farcs01808 \pm 0\farcs00076$.

1. INTRODUCTION

Stellar masses are one of the fundamental quantities in stellar astronomy. However, masses of only somewhat more than 100 stars have been directly measured to better than ~15% accuracy (e.g., Popper 1980), and the number of well-determined masses is growing only slowly. In this paper, we present masses determined from discrete-element interferometry for the components of α Equulei, a system whose angular separation is too small to have been measured with other techniques.

Observations of the orbits of binary stars offer the only direct way of measuring stellar masses. Until recently, the lower limit on measurements of separations of binary components has been 30–40 milliseconds of arc (mas) with speckle interferometry, precluding measurements of the apparent orbits of a number of nearby bright systems. With modern discrete-element optical interferometry, it is possible to surpass this limit. Since early 1989, we have been carrying out a program of observations of spectroscopic binaries with the Mark III Optical Inteferometer on Mt. Wilson. The 31.5 m maximum base line makes it possible to measure separations as small as 4 mas; thus, we have concentrated on binaries with expected separations, based on spectral types, periods, and apparent magnitudes, between 4 and 40 mas. In this paper, we present results for α Equulei, including orbital elements, masses, and the magnitude differences at four wavelengths. We combine the magnitude differences with the observed composite colors to constrain the range of spectral types of the components, and compare the absolute magnitudes and the individual colors to those of evolutionary models to constrain the age and metallicity of the system.

Alpha Equulei (=FK4 800=HR 8131=HD 202447/8; α, δ [1950] $= 21^{\rm h}13^{\rm m}19\overset{\rm s}{.}440, +5°2'24\farcs35$; $m_V = 3.92$) is a double-lined spectroscopic binary (Deutsch 1954; Stickland 1976; Pike 1978; Rosvick & Scarfe 1991) listed in the compilations of Batten *et al.* (1989) and Pédoussant *et al.* (1988). Previous work has reported spectral types G2 III and A5 V (Levato 1975; Stickland 1976; Stickland 1988) for the components, while Rosvick & Scarfe comment that the type of the G component seems to be closer to that of

[1]Universities Space Research Association (USRA), Washington Office Center, 409 Third St. SW, Suite 330, Washington, DC 20024.
[2]Mailing address: NRL/USNO Optical Interferometer Project, Center for Advanced Space Sensing, Naval Research Laboratory, Code 4215, Washington, DC 20375.
[3]Present address: Raman Research Institute, Bangalore 560080, India.
[4]SFA Inc., 1401 McCormick Dr., Landover, MD 20785.
[5]The Mark III Optical Interferometer, located on Mt. Wilson near Los Angeles, CA, is jointly operated by the Center for Advanced Space Sensing of the Naval Research Laboratory (NRL) and the U. S. Naval Observatory (USNO).

 0004-6256/92/070241-12$00.90 © 1992 Am. Astron. Soc.

© American Astronomical Society • Provided by the NASA Astrophysics Data System

1992AJ....104..241A

β Bootis (G8 III) than to that of 24 Ursae Majoris (G2 IV). The most precise reported period $P=98^{d}800 \pm 0^{d}004$ (Rosvick & Scarfe 1991). The trigonometric parallax has been variously reported between $\pi_{trig}=0''.013 \pm 0''.005$ (cited by Stickland 1976) and 0".021 in the *Yale Bright Star Catalog* (Hoffleit & Jaschek 1982). The parallax reported here, which is derived from combining the spectroscopic and interferometric results and for which the term "kinematic parallax" or π_{orb} has been suggested, is given by $\pi_{orb}=0''.01808 \pm 0''.00076$, consistent with the range of π_{trig}.The composite nature of the spectrum was noted by Maury & Pickering (1897); the first velocity variations were noted by Wright (Campbell 1902); and the initial spectral types of F8+A3 were given by Cannon & Pickering (1924). Unsuccessful attempts to measure the separation of the components interferometrically were made by Merrill (1922), McAlister (1978), Bonneau *et al.* (1980), and Hartkopf & McAlister (1984).

The initial spectroscopic observations (Deutsch 1954) suggested that the more-evolved G star was the less massive, a result also found by Stickland (1976). This posed a puzzle, since the system is thought to be too wide for mass transfer to have occurred. Vansina & de Grève (1982) derived various parameters for a number of systems, using for α Equulei the mass ratio and spectral types reported by Stickland (1976). They concluded that the primary does fill its Roche lobe, and inferred a large magnitude difference of $5^{m}5$ and masses of 1.77 and 1.85 $\mathcal{M}_{\odot}$ for the G and A stars, respectively.

However, reanalysis of Stickland's data by Pike (1978), as well as a further set of observations by Rosvick & Scarfe (1991) with more-precise radial velocity data, showed that the G primary is the more massive star after all ($\mathcal{M}_G/\mathcal{M}_A = 1.147 \pm 0.046$; Rosvick & Scarfe 1991), and thus, that invoking neither mass transfer nor a contact system is necessary. The results reported here lend additional indirect support to this interpretation: If we accept Pike's and Rosvick and Scarfe's results that the G star is the more massive, the masses and magnitude differences reported here are consistent, in the framework of the evolutionary models of VandenBerg (1985), with a detached system consisting of components of equal age and initial metallicity.

2. THE MARK III INTERFEROMETER

The Mark III interferometer has been described in some detail by Shao *et al.* (1988) and by Mozurkewich *et al.* (1991). A briefer description is included here. The configuration since mid-1988 has included five 25 cm siderostats, with two in use at any given time. The three siderostats for astrometric observations are on fixed piers that can be combined for either a 12 m north–south baseline or a 12 m east-south baseline. Two more siderostats, used for the observations described here, can be transported among a set of 12 piers along a north–south line to allow 36 baselines with lengths between 3.0 and 31.5 m. Light is transmitted from the siderostats to the optics lab through evacuated pipes to suppress ground seeing and dispersion effects. The full aperture is 7.5 cm in diameter, of which the inner 5 cm diameter is used for fringe detection and the outer annulus is used for star tracking. This results in a sensitivity limit of $\sim 4^{m}5$ for both star tracking and fringe detection. Sky coverage for each of the longest baselines is restricted by the maximum of ±10 m of optical delay available and by the asymmetry of the placement of the siderostats with respect to the optics lab.

In the optics lab, light from each siderostat traverses its own delay line, consisting of a cat's-eye retroreflector—a parabolic mirror with a flat at the focus—moving in an evacuated pipe. The flats are mounted on piezoelectric stacks for tracking fast fringe motions in the north/east delay line and for delay modulation in the south delay line. The north delay line searches for fringes and tracks them with a three-level servomechanical loop driving the retroreflector motor for low frequencies, a voice coil for intermediate frequencies, and the piezoelectric stack for high frequencies. Delay-line positions are measured with laser interferometry.

The stellar light beams are combined at a beamsplitter, resulting in two combined beams. The outer annulus of one of the combined beams is directed to a PAPA camera for tracking image motion due to the atmosphere and siderostat tracking errors. Light from the inner 5 cm of each of the combined beams is split by a dichroic and focused onto two optical fibers. The resulting four channels comprise the broadband (650–900 nm) fringe-detection channel and three narrowband (typically 25 nm) data channels. The detectors for the narrowband channels are cooled phototubes. For the broadband channel, a cooled phototube was used until mid-1989, when it was replaced with a photon-counting avalanche photodiode, resulting in an increase in sensitivity of about 1 mag.

The delay-line piezoelectric stack modulates the delay with a triangle wave of 800 nm amplitude and 4 ms effective period. Photons detected synchronously with this triangle wave modulation are used to calculate the fringe phase, which is then used as the error signal to adjust the north delay line. Off-line, the squared visibility amplitude V^2 and phase are estimated and averaged in 0.5 s records. We use an unbiased estimator of V^2; no unbiased estimator is known for V.

A typical night of observing consists of numerous cycles through an observing list of 10–20 stars, of which slightly less than half are calibrators, i.e., single stars with uniform-disk diameters less than ~1.5 mas (most are less than 1 mas). After the stellar image is acquired, fringes are searched for. When they are found, the system continues taking data for a scan of fixed length, usually 75 s. The siderostats are then slewed to a position 1° away, and a 5 s background flux and dark count measurement is made. About 100–200 scans can be done on a typical night; when the seeing is particularly good so fringes are easy to find, as many as 225 scans may be done.

3. OBSERVATIONS

Observations of α Equulei were carried out on 35 nights during 1989 and 1990. Six nights yielded too few scans to

© American Astronomical Society • Provided by the NASA Astrophysics Data System

1992AJ....104..241A

TABLE 1. Observation log.

UT Date (1)	BY[a] (2)	ϕ_{orb} (3)	BL[b] (m) (4)	N_{obs} (5)
1989				
Jun 13	0.4493	1.0008	23.7	8
Jun 18	0.4628	1.0506	20.4	20
Jun 21	0.4712	1.0816	20.4	18
Jun 23	0.4766	1.1018	20.4	16
Jul 08	0.5177	1.2536	17.0	10
Jul 13	0.5313	1.3039	3.7	16
Aug 08	0.6021	1.5656	7.2	10
Aug 09	0.6050	1.5762	7.2	16
Aug 13	0.6159	1.6166	10.0	16
Aug 20	0.6349	1.6869	13.5	15
Aug 23	0.6430	1.7168	13.5	20
Aug 27	0.6540	1.7575	23.7	5
Sep 15	0.7060	1.9498	20.2	7
Oct 14	0.7854	2.2431	7.2	11
Oct 17	0.7934	2.2729	10.0	5
Oct 18	0.7961	2.2829	10.0	12
Nov 02	0.8373	2.4352	23.7	4
Nov 06	0.8482	2.4752	20.4	18
1990				
Jun 26	0.4840	4.8259	10.0	7
Jun 28	0.4896	4.8463	10.0	7
Jul 29	0.5743	5.1596	23.7	11
Jul 30	0.5770	5.1696	23.7	12
Aug 01	0.5824	5.1894	23.7	14
Aug 27	0.6536	5.4526	23.7	12
Aug 30	0.6616	5.4825	20.4	19
Aug 31	0.6644	5.4928	20.4	17
Sep 02	0.6698	5.5126	17.0	21
Sep 03	0.6727	5.5233	13.5	13
Sep 15	0.7054	5.6442	13.5	20

[a]Fractional Besselian year
[b]Projected baseline at transit

be useful. Baseline lengths varied from 4.2 to 27.0 m; the maximum baseline length of 31.5 m cannot be used for $\delta < 7.^{\circ}8$. Observations were carried out with data channels at $\lambda\lambda$ 800, 550, and 450 nm in 1989, and at $\lambda\lambda$ 800, 550, and 500 nm in 1990. Filter widths were 22 nm for λ800 nm and 25 nm for the other filters. Table 1 is a log of the observations. Column (1) gives the UT observation data; column (2) the mean weighted fractional Besselian year; column (3), the orbital phase; column (4), the projected base-line length at transit; and column (5), the number of scans remaining after editing.

4. DATA EDITING AND CALIBRATION

The method we used for editing and calibrating a night's data from the Mark III is described in detail by Mozurkewich *et al.* (1991) and summarized here. Editing the data included a number of steps, the first of which was background subtraction. Polynomials in time and delay were fit to the background counts in each channel; scans for which the background flux deviated from the fit by more that 3% of the stellar flux were deleted. The measured background counts (not the estimated counts from the polynomial fit) were subtracted from each surviving scan. In the second step, we calibrated the sensitivity of the detectors using the observed photon rates for all stars observed on each night and their magnitudes from the *Bright Star Catalog*. We deleted scans from the flux calibration for which the stellar flux differed from the expected value by more than $\sim 0^{m}3$. In the third step, we deleted 0.5 s records in which the number of detected photons deviated by more than 3σ from the mean for that scan. For the fourth and final step, we deleted 0.5 s records within each scan that were identified as having been taken when the fringe tracker error was more than two fringes. We did not run a median filter over the values of V^2.

The final product of the editing process is a set of observed squared visibility amplitudes and uncertainties for each scan and wavelength. The uncertainties were estimated from the rms scatter of the 0.5 s records within each scan.

In order to calibrate Mark III data, one must estimate, for each observing wavelength, the system squared visibility amplitude, V^2_{sys}, defined as the squared visibility amplitude of an unresolved star as observed with the real instrument. Under the best observing conditions, $V^2_{sys} \approx 0.72$ for the λ800 nm channel with a 2.5 cm aperture, but smaller values are seen for shorter wavelengths and larger apertures, and there are large variations during and between nights. Once V^2_{sys} is estimated as a function of, for example, seeing, zenith angle, or time, the corrected squared visibility amplitudes can be calculated.

We estimated V^2_{sys} from the observed squared visibilities, V^2_c, of the calibrator stars described in Sec. 2, setting $V^2_{sys} = V^2_c / V^2_{est}$, where V^2_{est}, the squared visibility of the calibrators as observed with a perfect instrument, is calculated from their uniform-disk diameters. The uniform-disk diameter $D(\lambda)$ is the diameter of the uniformly bright disk that gives the same visibility as the real stellar disk. It differs from the true angular diameter because of limb darkening, which varies with λ. Diameters for the calibrators were estimated with the procedure given by Mozurkewich *et al.* (1991), which uses the $(R-I)_J$ color (the subscript indicates the Johnson system) and m_V.

Much of the variation in V^2_{sys} correlates with the seeing index (approximately the rms fringe motion during a scan; see Mozurkowich *et al.* 1991). We fit a quadratic to V^2_{sys} as a function of the seeing index, with the function constrained to have zero slope for perfect seeing. A similar quadratic was fit to the variations of V^2_{sys} with zenith angle. The remaining variations of V^2_{sys} with time were boxcar-smoothed with a 2 hr time constant. We then used the estimate of V^2_{sys} as a function of seeing, zenith angle, and time that results from this process to obtain corrected squared visibility amplitudes: $V^2_{corr} = V^2_{obs} / V^2_{sys}$.

The V^2_{corr} of the calibrators and their estimated squared visibilities, V^2_{est}, can be used to check for remaining systematic effects and to evaluate the calibration uncertainty. We evaluated a calibration constant $C_\lambda \equiv \langle V^2_{corr} / V^2_{est} \rangle$, where the angle brackets indicate averaging over all the calibrator scans during the night, which corresponds to the zero-base-line visibility. By construction, $C_\lambda = 1$. The scatter of V^2_{corr} / V^2_{est} about C_λ is due to random variations of V^2_{obs}, which result in a random error in V^2_{sys}, and to remaining systematic errors in V^2_{sys}. The reduced χ^2 of the fit to C_λ is a measure of the size of the remaining systematic errors in comparison to the uncertainties in V^2_{obs}.

We estimated the calibration uncertainty σ_{C_λ} as the un-

© American Astronomical Society • Provided by the NASA Astrophysics Data System

1992AJ....104..241A

certainty which, when added in quadrature to all the individual V^2 uncertainties, resulted in lowering the reduced χ^2 to unity; however, we assumed that σ_{C_λ} was never less than 0.01. In general, the rms scatter of calibrator $V^2_{\rm corr}$ was smaller than the typical uncertainty in $V^2_{\rm obs}$, indicating that the systematic effects remaining after calibration were small. Typical values for the calibration uncertainties were 0.01 at λ800 nm, 0.015–0.05 at λ550 nm, and 0.03–0.10 at $\lambda\lambda$ 500 nm and 450 nm.

5. DATA ANALYSIS

The goal of the data analysis for a binary is a set of position angles and separations for each observed epoch, from which we can derive the orbit, and the magnitude difference between the components at each wavelength, from which we can infer the colors of the components. The angular diameters of the components are usually too small to determine reliably from our data, and must be estimated separately.

We analyzed the data in a two-step procedure: (1) analysis of data from single nights, and (2) analysis of the ensemble of separation-position angle measurements. The first pass through this procedure yielded preliminary results: step (1) used initial estimates of the magnitude differences $\Delta m(\lambda)$ and diameters $D_{1,2}$ to determine the separations ρ and position angles θ; step (2) used these (ρ, θ) pairs to estimate preliminary orbital elements.

On the second pass through the procedure, we held the (ρ, θ) pairs from the orbital solution fixed and used step (1) to produce refined estimates of $\Delta m(\lambda)$. These $\Delta m(\lambda)$ were then used to reestimate $D_{1,2}$. We found that the estimates of $D_{1,2}$ did not change. We then held $\Delta m(\lambda)$ fixed at the new values and used step (1) again to obtain new estimates of ρ and θ. The second pass continued with step (2) to obtain a new orbital solution. The changes in the orbital elements were smaller than the uncertainties, so we judged that the procedure had converged. The next subsections describe steps (1) and (2) in more detail.

5.1 Parameters in Fits to Data from a Single Night

The squared visibility amplitude V^2 of a binary star is a set of fringes in the (u, v) plane whose separation is proportional to $1/\rho$ and whose position angle is $\theta+\pi/2$. One fringe maximum must pass through $(u, v)=(0, 0)$. At a given wavelength, the visibility amplitudes of the individual components are given by

$$V_{1,2}=\frac{2J_1(\pi D_{1,2}B_\lambda)}{(\pi D_{1,2}B_\lambda)}\approx 1-\frac{(\pi D_{1,2}B_\lambda)^2}{8}, \quad (1)$$

where J_1 is the Bessel function of the first kind, $D_{1,2}$ are the uniform-disk diameters at this wavelength, and B_λ is the projected baseline length in wavelengths. The maximum and minimum squared visibility amplitudes of the binary are

$$V^2_{\rm max,min}=\left(\frac{FV_1\pm V_2}{F+1}\right)^2, \quad (2)$$

where $F=S_1/S_2$, the ratio of the fluxes of the two components. From Eqs. (1) and (2) it can be seen, for example, that the contrast between maximum and minimum V^2 decreases with increasing D_2, which decreases V_2^2, or with increasing $\Delta m(\lambda)$ (i.e., increasing F).

The total number of parameters we could fit to one night's binary visibilities from the Mark III is thus 14. The first nine are $\Delta m(\lambda)$, $D_1(\lambda)$, and $D_2(\lambda)$ for each of three wavelengths. The remaining five are ρ, θ, and the calibration constants C_λ described in Sec. 4 above: allowing C_λ to vary during the fitting procedure reflects the existence of the calibration uncertainty. The number of parameters we actually fit, however, was never more than eight; diameters were not fit, but were estimated as described below.

We used the Marquardt-Levenberg nonlinear least-squares algorithm as given by Press *et al.* (1986) to fit the parameters. The model used to calculate the visibilities is given in the Appendix. Model visibilities were calculated for all wavelengths simultaneously, with one component at the phase center (the G component in this case, since it is $1^{\rm m}2$ brighter at the fringe-tracking wavelength) and the second offset by ρ and θ. The greatest fractional bandwidth in the data channels was 5.5%.

The algorithm reliably found the minimum χ^2 at the same point in parameter space with a variety of initial parameters. We tested the robustness of the algorithm for several nights' data by using separate gradient search and curvature fitting algorithms based, respectively, on the programs GRADLS and GRIDLS in Bevington (1969). The results from the three methods were always in agreement. Figure 1 shows examples of observed squared visibilities and best fits for the best night and for a typical night.

It is straightforward to find solutions for ρ and θ from data from a single night and a single wavelength when, as in this case, $\Delta m(\lambda)$ is small (so the fringe contrast is significantly greater than the uncertainty in V^2) and the (u, v) track traverses one complete fringe or more. Vivekanand (1990) has pointed out that multiple solutions for ρ and θ are possible for single-wavelength data, especially if the (u, v) track is nearly straight. However, if data for two or more wavelengths are available, the ambiguity is nearly always resolved. For all of the nights listed in Table 1, data were obtained at two or more wavelengths, and only one solution per night was found to fit the data.

5.2 Diameter Estimates

The diameters $D_{1,2}(\lambda)$ are poorly determined by our data, since the G component of α Equulei is only slightly resolvable by the Mark III, and the A component is unresolvable. Rather than attempting to fit diameters, we used diameter estimates as fixed parameters in our fitting process. Our first estimates were obtained from preliminary estimates for the magnitudes $m_{V,\rm A}$ and $m_{V,\rm G}$, which in turn were derived from the combined magnitude in the *Bright Star Catalog* and the Δm_V $(=M_{\rm A,V}-M_{\rm G,V})$ interpolated in tables in Allen (1976) for the spectral types given by Stickland (1976). Values for $(R-I)_{\rm J}$ were also taken from tables in Allen (1976) by interpolation. From these

© American Astronomical Society • Provided by the NASA Astrophysics Data System

1992AJ....104..241A

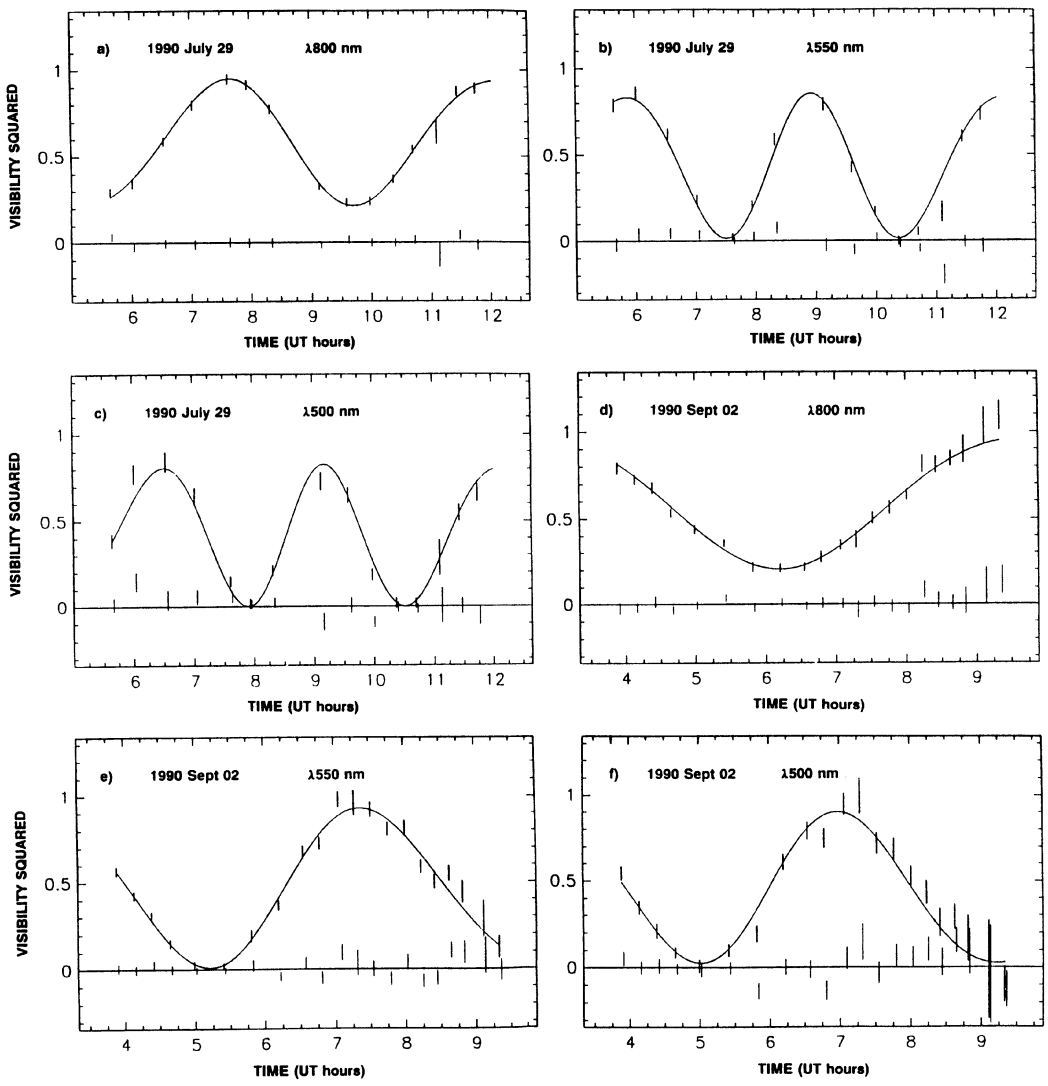


FIG. 1. Plots of V^2 as a function of time for two nights. (a)–(c): data at $\lambda\lambda$ 800, 550, and 500 nm for 1990 July 29, the night that gives the smallest errors in ρ and θ. The error bars shown are $\pm 1\sigma$; the lighter error bars show the residuals, also with $\pm 1\sigma$ errors. (d)–(f): as in the previous panels, but with data for 1990 September 02, a night that gives typical uncertainties in ρ and θ.

$\Delta m(\lambda)$ and $(R-I)_J$ we calculated D_G (800 nm) = 1.50 mas, D_G (450 nm) = 1.43 mas, and D_A (800 nm) = D_A (450 nm) = 0.4 mas, using the procedure given by Mozurkewich *et al.* (1991) (see Sec. 4 above).

We used improved measurements of $\Delta m(\lambda)$ from the second pass through the analysis procedure to obtain new diameter estimates. We fixed ρ and θ in step (1) at their values from the orbital fit, found new best-fit values for Δm(550 nm), and derived new values for $m_{V,A}$ and $m_{V,G}$. New values for $(R-I)_J$ were then derived by two methods. In the first, the spectral types that best fit the measured $\Delta m(\lambda)$ and published m_V were determined, and the $(R-I)_J$ colors obtained from Johnson's (1966) tables (see Sec. 6). In the second, we used the colors of the system (Stickland 1976), and Δm_R and Δm_I interpolated from our Δm(550 nm) and Δm(800 nm) to estimate $(R-I)_J$ directly. For the G star, the two methods yielded $(R-I)_J = 0^m.48$ and $(R-I)_J = 0^m.495 \pm 0^m.02$, respectively; we adopted $(R-I)_J = 0^m.49 \pm 0^m.03$. For the A star, the two methods gave $(R-I)_J = 0^m.06$ and $(R-I)_J = -0^m.08 \pm 0^m.04$; we adopted $(R-I)_J = 0^m.00 \pm 0^m.06$. The final estimates of D(800 nm) and $D(\lambda)/D$(800 nm) for both components are listed in Table 2, including uncertainties from the $(R-I)_J$ uncertainties for each star. The diameter estimates for the G component increased by ~1.5% from the preliminary estimates, corresponding to a decrease in V^2 of only 0.6% at λ450 nm. At λ450 nm on the longest base line, a 1σ error in D corresponds to a 2.1% or a 0.4% change in V^2 for the G and A components, respectively. The estimated diameters are well below the Roche limit of 35%–40% of the ~12 mas orbital separation determined

© American Astronomical Society • Provided by the NASA Astrophysics Data System

1992AJ....104..241A

TABLE 2. Comparison of calibration constants from calibration stars and from α Equulei.

Date	Calibration Uncertainties (1σ) from Calibration Stars			Calibration Constants C_λ and Uncertainties (1σ) from α Equulei		
	800 nm	550 nm	450 nm	800 nm	550 nm	450 nm
1989						
Jun 13	0.010[a]	0.010	0.023	1[b] ±0.025	1 ±0.033	1 ±0.357
Jun 18	0.016	0.014	0.044	1 ±0.010	1 ±0.019	1 ±0.085
Jun 21	0.083	0.049	0.157	1.066±0.025	1.014±0.013	1.094±0.066
Jun 23	0.024	0.050	0.010	1.024±0.013	1.020±0.020	1.043±0.182
Jul 08	0.010	0.014	0.083	1.010±0.038	1.035±0.165	0.986±0.228
Jul 13	0.010	0.019	0.043	0.990±0.039	0.057±0.078	1.089±0.879
Aug 08	0.010	0.050	0.031	1.010±0.024	1.015±0.034	1.031±0.123
Aug 09	0.010	0.010	0.073	0.985±0.014	1.017±0.051	1.076±0.089
Aug 13	0.010	0.028	0.073	0.999±0.013	1.017±0.027	
Aug 20	0.010	0.061	0.133	0.990±0.026	1.118±0.062	
Aug 23	0.043	0.038	0.045	1.023±0.026	1.027±0.032	
Aug 27	0.010	0.010	0.010	1.010±0.056	1.010±0.091	
Sep 15	0.010	0.028	0.035	0.990±0.035	0.972±0.975	0.965±0.111
Oct 14	0.027	0.069	0.105	0.973±0.985	0.931±0.413	0.943±0.275
Oct 17	0.013	0.027	0.061	1.013±0.046	1.027±0.036	
Oct 18	0.011	0.032	0.050	0.989±0.036	1.032±0.021	1.016±0.087
Nov 02	0.010	0.016	0.014	1 ±0.034	1 ±0.060	1 ±0.234
Nov 06	0.010	0.026	0.043	1.010±0.013	1.026±0.035	1.043±0.065
	800 nm	550 nm	500 nm	800 nm	550 nm	500 nm
1990						
Jun 26	0.013	0.035	0.072	1 ±0.056	1 ±0.022	1 ±0.059
Jun 28	0.058	0.110	0.095	1 ±0.080	1 ±0.045	1 ±0.090
Jul 29	0.010	0.028	0.049	1.010±0.018	0.989±0.027	0.986±0.034
Jul 30	0.015	0.035	0.067	1.011±0.026	0.993±0.044	1.025±0.045
Aug 01	0.012	0.032	0.053	0.991±0.024	0.984±0.028	0.994±0.046
Aug 27	0.010	0.026	0.065	1.005±0.021	1.009±0.019	1.031±0.048
Aug 30	0.010	0.037	0.075	1.010±0.016	1.030±0.025	1.012±0.040
Aug 31	0.010	0.031	0.072	1.008±0.012	0.990±0.022	0.985±0.033
Sep 02				1.011±0.021	0.999±0.019	0.993±0.032
Sep 03	0.011	0.019	0.053	1.010±0.031	0.985±0.028	1.033±0.033
Sep 15	0.018	0.038	0.094	1.018±0.017	1.023±0.021	1.001±0.037

[a] Uncertainties were assumed to be at least 0.010
[b] If $C_\lambda \equiv 1$, C_λ was not varied in the fit

below, further confirming that this is not at present a contact system.

Since it is important to know whether α Equulei is a mass-transfer system, it is useful to have a check on these diameters. We examined the dependence on base-line length of the $\Delta m(\lambda)$ and C_λ resulting from fits using these diameter values. To first order, if one of the actual diameters were larger than our estimate, the fitted $\Delta m(\lambda)$ would have declined quadratically with base-line length, while if both components were larger, C_λ would have declined with base line. Diameter errors at the ~15% level for the G star or the factor ~2 level for the A star would have been detectable; however, no dependence of $\Delta m(\lambda)$ or C_λ was found to be within the noise.

5.3 Magnitude Differences

The magnitude differences $\Delta m(\lambda)$, which we use to determine the colors of the components, were determined directly from the data. For preliminary estimates, we used data from the eleven nights with the best signal-to-noise ratio and best coverage of both fringe maxima and minima, and fit the data for ρ, θ, $\Delta m(\lambda)$, and C_λ, using the preliminary estimates of $D_{1,2}(\lambda)$ described above. In the second round of fitting individual nights' data, ρ, θ, and $D_{1,2}(\lambda)$ were held fixed, and $\Delta m(\lambda)$ from all nights were obtained.

The results of fitting $\Delta m(\lambda)$ for the observed wavelengths and estimating Δm at the Cousins I_C and R_C bands (Cousins 1976a,b, 1978; Bessel 1976, 1979) and the Johnson V and B bands are shown in Table 3. Because the signal-to-noise ratio for Δm(450 nm) is poor, we used a linear fit to the λλ450, 500, and 800 nm magnitude differences to generate the adopted $\Delta m(\lambda)$ for 450 nm $< \lambda \leqslant$ 550 nm shown in Table 3. For 550 nm $< \lambda <$ 800 nm, the $\Delta m(\lambda)$ in Table 3 are an interpolation between Δm(550 nm) and Δm(800 nm). These were the $\Delta m(\lambda)$ that were used in estimating final values for $D_{1,2}(\lambda)$ and in fitting final values for ρ and θ. Because $D_{1,2}(\lambda)$ and the orbital elements did not change significantly with the new values of $\Delta m(\lambda)$, the new magnitude differences were adopted.

© American Astronomical Society • Provided by the NASA Astrophysics Data System

1992AJ....104..241A

TABLE 3. Diameters and magnitude differences.

Parameter	Wavelength (nm) or Band							
	800	789 I_C	653 R_C	550	547 V	500	450	435 B
Adopted Uniform-Disk Diameters								
D_G (mas)	1.5[a]							
$D_G/D_G(800)$				0.95[b]		0.95[b]	0.95[a]	
D_A (mas)	0.35[a]							
$D_A/D_A(800)$				1.0[b]		1.0[b]	1.0[a]	
Measured Magnitude Differences								
$m_A - m_G$	1.m20 ±0.03			0.m47 ±0.06		0.m31 ±0.16	-0.m4 ±0.3	
Adopted Magnitude Differences								
$m_A - m_G$	1.m20 ±0.03	1.m17 ±0.03	0.m78 ±0.05	0.m47 ±0.06	0.m46 ±0.06	0.m17 ±0.11	-0.m15 ±0.16	-0.m24 ±0.19

[a] Diameters at λ800 nm and λ450 nm calculated as in Mozurkewich et al. 1991
[b] Adopted from λ450 nm value

5.4 Separations and Position Angles

Separations and position angles are the most important quantities to be determined from each night's data. Initial values for ρ and θ for each night were found either by examining the locations of V^2 maxima in (u, v) or by using the values from a night with similar orbital phase. For finding both preliminary and final nightly values of ρ and θ to use in fitting the orbit, we varied ρ, θ, and $C_{\lambda_1,\lambda_2,\lambda_3}$, with $\Delta m(\lambda_1,\lambda_2,\lambda_3)$ and $D_{1,2}(\lambda_1,\lambda_2,\lambda_3)$ fixed at their preliminary or final adopted values, respectively. For some nights, the number of measured visibilities was too small to justify C_λ. In those cases, we assumed that the calibration was perfect ($C_\lambda = 1$) and solved only for ρ and θ. These fits were used in the subsequent orbit fitting, but

TABLE 4. Single-night fits.

UT Date (1)	Fractional Besselian Year (2)	ρ (mas) (3)	θ (deg) (4)	σ_{maj} (mas) (5)	σ_{min} (mas) (6)	ϕ_{err} (deg) (7)	$\alpha_{(O-C)}$ (mas) (8)	$\delta_{(O-C)}$ (deg) (9)	Notes (10)
1989									
Jun 13	0.4493	9.63	126.6	1.94	0.081	90.9	- 1.00	0.031	1, 4
Jun 18	0.4628	10.30	103.0	0.45	0.049	104.5	- 0.33	0.091	1, 5
Jun 21	0.4712	10.62	90.7	1.23	0.095	90.8	- 0.24	0.028	1, 5
Jun 23	0.4766	10.38	82.3	3.19	0.16	94.7	- 0.67	0.08	1, 5
Jul 08	0.5177	12.39	33.8	3.84	0.57	80.6	0.52	0.14	1, 5
Jul 13	0.5313	11.79	18.3	3.69	2.24	114.8	0.41	- 0.19	1, 6
Aug 08	0.6021	10.25	276.7	2.51	0.48	106.5	0.55	- 0.26	1, 4
Aug 09	0.6050	10.76	272.2	1.39	0.36	88.9	0.14	- 0.27	1, 5
Aug 13	0.6159	11.33	258.0	0.99	0.18	88.6	- 0.05	- 0.13	2, 6
Aug 20	0.6349	11.55	233.5	0.45	0.22	78.1	0.34	- 0.04	2, 6
Aug 23	0.6430	11.62	221.5	1.13	0.22	108.2	0.74	- 0.25	1, 6
Aug 27	0.6540	12.36	216.0	2.86	0.10	99.4	- 0.90	0.16	2, 4
Sep 15	0.7060	10.55	144.1	2.06	0.24	85.5	0.00	0.09	1, 5
Oct 14	0.7854	11.21	29.6	4.10	1.65	74.4	- 1.42	- 0.01	1, 5
Oct 17	0.7934	12.98	33.2	3.04	0.63	75.4	1.86	0.11	1, 5
Oct 18	0.7961	11.28	21.8	1.39	0.38	77.9	- 0.44	- 0.53	1, 5
Nov 02	0.8373	10.85	330.2	0.94	0.091	69.9	0.04	0.067	2, 6
Nov 06	0.8482	10.66	314.5	0.73	0.085	76.1	0.06	0.100	1, 5
1990									
Jun 26	0.4840	11.95	190.2	1.35	0.22	103.7	- 0.09	- 0.26	3, 4
Jun 28	0.4896	13.01	162.0	4.72	0.74	93.2	4.63	- 0.88	3, 4
Jul 29	0.5743	11.48	62.4	0.15	0.042	86.4	- 0.10	- 0.003	3, 7
Jul 30	0.5770	11.73	59.7	0.33	0.080	88.8	0.12	- 0.028	3, 7
Aug 01	0.5824	11.79	52.8	0.26	0.059	94.9	0.02	- 0.018	3, 7
Aug 27	0.6536	10.68	323.4	0.19	0.041	82.4	0.10	0.018	3, 7
Aug 30	0.6616	10.47	311.1	0.41	0.079	86.3	0.13	- 0.062	3, 7
Aug 31	0.6644	10.52	307.1	0.29	0.054	85.8	0.10	0.005	3, 7
Sep 02	0.6698	10.54	298.7	0.20	0.050	96.2	0.06	- 0.033	3, 7
Sep 03	0.6727	11.41	292.4	0.66	0.086	81.4	- 0.87	- 0.043	3, 7
Sep 15	0.7054	11.92	249.7	0.34	0.081	84.4	- 0.46	- 0.006	3, 7

Notes:
1. 800, 550, 450 nm data used
2. 800, 550 nm data used
3. 800, 550, 500 nm data used
4. Fit r, θ
5. Fit r, θ, C_{800}, C_{550}, C_{450}
6. Fit r, θ, C_{800}, C_{550}
7. Fit r, θ, C_{800}, C_{550}, C_{500}

© American Astronomical Society • Provided by the NASA Astrophysics Data System

1992AJ....104..241A

TABLE 5. Best-fit orbital elements.

Parameter	Value	Uncertainty (1σ)	Previous Results	Reference
a	11.987 mas	± 0.078		
e	0.0056	± 0.0034	0.037 ± 0.027	Pike 1978
P	98^d.800 (adopted)		98^d.800 ± 0^d.004	Rosvick & Scarfe 1991
T	JD 2447592.1 (= BY 1989.18)	+3^d.6/−10^d.1 (+0.01/−0.03 yr)	JD 2441567.8 ± 8^d.0 JD 2443614.35 ± 0^d.08[b]	Pike 1978 Rosvick & Scarfe 1991
i	151°.5	± 1°.1		
Ω	33°.9	± 2°.2		
ω	270°[c]	+14°/−37°	35° ± 48° 105° ± 29°	Stickland 1976 Pike 1978

[a]Epoch of osculation = BY 1990.465
[b]Rosvick & Scarfe 1991 value is T_0 (maximum radial velocity) rather than T (periastron passage)
[c]180° ambiguity in Mark III results; spectroscopic and visual conventions differ by 180°

they have significantly larger uncertainties, and so contribute only weakly to the fitted orbital parameters. Table 4 shows results of the fits to each night's data: column (2) gives the fractional Besselian year; columns (3) and (4) give the best-fit separation ρ and position angle θ; columns (5)–(7) give the major and minor axes and position angle of the 1σ error ellipse. Columns (8) and (9) give the differences between the observed and calculated separations; these are resolved into right ascension and declination differences for more direct comparison with the major and minor axes of the error ellipse, since the ellipse is usually oriented nearly east–west. The notes cited in column (10) give the wavelengths analyzed and the parameters fit for each night.

5.5 *Uncertainty Estimates for Single-Night Parameters*

The uncertainty ellipse for ρ and θ given in Table 4 for each night is the projection of the 68% confidence surface in the space of the fitted parameters onto the $\Delta\rho$–$\Delta\theta$ plane. Points on this surface were found by increasing or decreasing a parameter and fitting the others until the χ^2 corresponding to the 68% confidence level was found, and repeating this for each parameter. We found that the best-fit ρ and θ change by significantly less than 1σ when the other parameters are increased or decreased to their 1σ values.

We compared these uncertainties in ρ and θ to those found from the diagonal elements of the covariance matrix, which also give the projections of a surface of constant χ^2 onto the $\Delta\rho$–$\Delta\theta$ plane. Using the covariance matrix assumes implicitly that χ^2 is paraboloidal in the neighborhood of the best fit. The covariance matrix method typically found uncertainties smaller than those of the first method by ~30%, which is a measure of the departure of the χ^2 surface from a paraboloid.

5.6 *Orbit Fitting*

For orbit determinations, the initial set of orbital elements was estimated by the Thiele-Innes method (see, e.g., Green 1985) from the set of (ρ, θ) pairs and uncertainties of Table 4, using the 98^d.800 period given by Rosvick & Scarfe (1991). We used a Marquardt-Levenberg nonlinear least-squares algorithm similar to that used to find the nightly separations and position angles to find the best-fit orbital elements: the semimajor axis a, ellipticity e, period P, epoch T, inclination angle i, position angle of the ascending node Ω, and argument of periastron ω. The algorithm with these data is quite robust: starting positions in parameter space differing by 50% in a, 1 rad in the angles, and/or 0.5 in e converged to the same solution. We found the 68% confidence contour in χ^2 with the same approach used in assessing the uncertainties in the single-night results, i.e., by varying one parameter until the best fit of the remaining parameters failed to reduce χ^2 to the 68% confidence level.

Fits were performed both by holding P fixed at 98^d.800 and by allowing P to vary; all the other elements were allowed to vary in both treatments. Allowing P to vary does not yield a significant improvement in the uncertain-

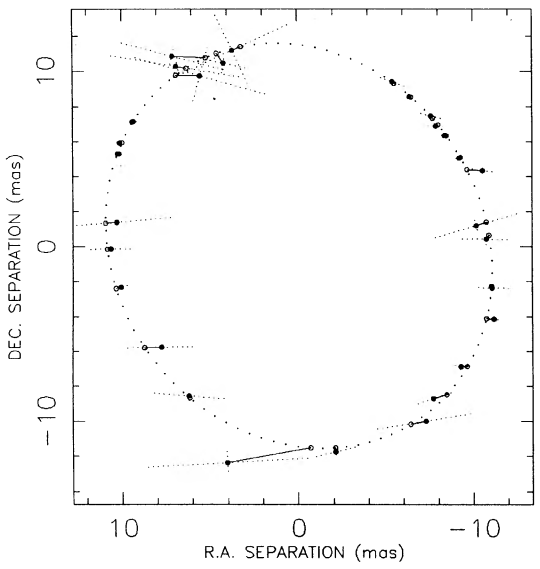


FIG. 2. The best-fit orbit for α Equulei as projected on the sky. The 1σ errors from Table 4 are shown.

© American Astronomical Society • Provided by the NASA Astrophysics Data System

1992AJ....104..241A

TABLE 6. System parameters.

Parameter	Value (±1σ)	Source of input parameters
$\mathcal{M}_G/\mathcal{M}_A$	1.147 ± 0.046	$K_{G,A}$: Rosvick & Scarfe 1991
$a_G \sin i$	2.205 ± 0.009 × 10^7 km	K_G, P: Rosvick & Scarfe 1991; e: this work
$a_A \sin i$	2.53 ± 0.10 × 10^7 km	K_A, P: Rosvick & Scarfe 1991; e: this work
$(a_G + a_A) \sin i$	4.73 ± 0.10 × 10^7 km	$K_{G,A}$, P: Rosvick & Scarfe 1991; e: this work
$a_G + a_A$	9.92 ± 0.40 × 10^7 km 0.663 ± 0.027 AU	$K_{G,A}$, P: Rosvick & Scarfe 1991; e, i: this work
$\mathcal{M}_G + \mathcal{M}_A$	3.99 ± 0.26 $\mathcal{M}_\odot$	$K_{G,A}$, P: Rosvick & Scarfe 1991; e, i: this work
D	55.3 ± 2.3 pc	$K_{G,A}$, P: Rosvick & Scarfe 1991;
π_{orb}	0".01808 ± 0".00076	e, i, a'': this work
$\mathcal{M}_G$	2.13 ± 0.29 $\mathcal{M}_\odot$	K_G, P: Rosvick & Scarfe 1991; e, i: this work
	2.36 — 2.75 $\mathcal{M}_\odot$	$M_{V,G}$, $(V - I_C)$: this work; evolutionary model: VandenBerg 1985
$\mathcal{M}_A$	1.86 ± 0.21 $\mathcal{M}_\odot$	K_A, P: Rosvick & Scarfe 1991; e, i: this work
	2.01 — 2.14 $\mathcal{M}_\odot$	$M_{V,A}$, $(V - I_C)$: this work; evolutionary model: VandenBerg 1985
$M_{V,G}$	0^m.75 ± 0^m.10	m_V: Hoffleit 1982; D, Δm_V: this work
$M_{V,A}$	1^m.21 ± 0^m.09	
age	0.5 — 0.6 Gyr	$M_{V,A}$, $(V - I_C)$: this work; evolutionary model: VandenBerg 1985
Z	$\sim Z_\odot$	

ties for the other orbital elements; the result, $P = 98^d.818 \pm 0^d.028$, is consistent with the $98^d.800 \pm 0^d.004$ period given by Rosvick & Scarfe (1991), but is less precise. Consequently, we adopted the orbital elements derived from fixing P at the Rosvick and Scarfe value. These elements and their 1σ uncertainties are listed in Table 5. The apparent orbit is shown in Fig. 2.

The referee has pointed out to us that the spectroscopic values for ω are based on the motion of the primary, while visual values are based on the motion of the secondary around the primary; consequently, determinations of ω from visual methods such as ours should differ from spectroscopic values by 180°. Because 180° can be added to both ω and Ω without changing the solution from our data, we give in Table 5 the (visual) value for ω from our data that is consistent with the (spectroscopic) value given by Pike (1978).

The value of e in our results is consistent with that of Pike; its difference from zero is only marginally significant in both studies. In that light, the agreement between our value of ω and Pike's is not very meaningful, nor is the agreement between Pike's T and our results.

6. RESULTS AND DISCUSSION

The most significant results of the present work are the determinations of the stellar masses, the distance, and the absolute magnitudes; these results are summarized in Table 6. In addition to the stellar masses, our data yield magnitude differences that can be used in conjunction with the composite magnitude and colors of the system to determine the colors, and hence the spectral types, of the components. Finally, M_V, obtained from m_V, Δm_V, and the distance, can be used with evolutionary models to constrain the ranges of age, mass, and metallicity for the system that are consistent with the data. Combining our results with the evolutionary model gives us a picture of α Equulei as a system with near-solar metallicity, and an age between 5 and 6.5×10^8 yr. As we discuss here, the masses of both the G and the A components from the evolutionary model are consistent with the orbital determination.

6.1 Masses, Absolute Magnitudes, Parallax, and Magnitude Differences

There are several constraints on the masses. The mass ratio $\mathcal{M}_G/\mathcal{M}_A$ is determined by K_A/K_G, the ratio of the projected orbital velocities from the spectroscopic data of Rosvick & Scarfe (1991). The masses of the individual components are determined by $K_{A,G}$, P, e, and $\sin i$. In addition, the uncertainty in the sum of the masses is smaller than the quadrature sum of their individual uncertainties, since the uncertainties in P, e, and i are present in both individual mass uncertainties.

Because P and e are well determined by both the spectroscopic data and our data, and because K_G is well determined by the spectroscopic data, most of the ~12% error in $\mathcal{M}_A$ and $\mathcal{M}_G$ is due to the uncertainties in i and K_A. The total mass is $3.99 \pm 0.26\ \mathcal{M}_\odot$, although as we discuss below the total mass of the system is likely to be at the upper end of that range in order to be consistent with the evolutionary models.

The orbital parallax, π_{orb}, is derived from our values of a'' and i and Rosvick & Scarfe's values of K_G and K_A (which give $a_{km} \sin i$) in the same way that Herbison-Evans *et al.* (1971) derived the distance to α Virginis. The

© American Astronomical Society • Provided by the NASA Astrophysics Data System

1992AJ....104..241A

result, $\pi_{orb}=0''.01808\pm0''.00076$, is consistent with the π_{trig} of $0''.013\pm0''.005$ quoted by Stickland, but with considerably improved precision. The resulting sum of the semimajor axes of the orbits of the two components is 0.663 ±0.027 AU. The absolute V magnitudes are also shown in Table 6. As with the masses, the errors in the separation, the parallax, and M_V are dominated by the uncertainties in K_G and K_A.

6.2 Colors and Spectral Types

The magnitude differences shown in Table 3 can be used with m_V and the combined colors given by Stickland (1976) to constrain the range of spectral types for each component. Two sets of constraints are available: the four measured magnitude differences at λλ 800, 550, 500, and 450 nm, and the four composite colors $(U-B)$, $(B-V)$, $(V-R)_J$, and $(V-I)_J$.

The set of magnitude differences yields a range of spectral-type pairs running roughly from G0 III+B9 V to K1 III+F0 V. For a given pair of types, fixing the magnitude difference at one wavelength determines the differences at other wavelengths. We fixed $\Delta m(800)$ at $1^m.20$ and interpolated in the tables in Johnson (1966) to find differences at λ550 nm (near V), λ500 nm, and λ450 nm (near B) for comparison to the measured $\Delta m(\lambda)$. The comparison for each of our wavelengths resulted in a region in the type-vs.-type plane in which the model $\Delta m(\lambda)$ are consistent with the data within $1.5\sigma_{\Delta m}$. The choice of this confidence level combines the uncertainty in our data with the spread of colors within a given subtype. The three allowed regions in the type-vs.-type plane for λλ 550, 500, and 450 nm overlap substantially, but with $\Delta m(450\text{ nm})$ allowing somewhat later types than $\Delta m(550\text{ nm})$ for the A star. Even though the uncertainty in $\Delta m(450)$ is large, it provides as good a constraint as $\Delta m(550)$ because of the greater wavelength difference between λ450 and λ800 nm.

The set of composite colors yields a range roughly perpendicular to the first range in the type-vs.-type plane. We calculated composite colors for the system, again using the Johnson (1966) tables, and using $\Delta m(\lambda 800\text{ nm})$ to adjust the relative contributions of the two stars. This is the same procedure used by Stickland (1976), but with the relative brightnesses of the components fixed. In the region in type-vs.-type space that runs from G0 III+F0 V to G5 III +A2 V, the rms deviation between the synthetic colors and the measured colors given by Stickland is less than $0^m.13$. Our best fit to the composite colors, G3 III+A7 V, is slightly different from Stickland's estimates of G2 III +A5 V (from comparison with Johnson's 1966 tables) and G3 III+A4 V (from comparison to model atmospheres).

The best fit to both the magnitude difference constraint and the composite color constraint is at G5 III+A5 V, close to both of Stickland's estimates. Rosvick & Scarfe (1991) note that subtraction of the spectrum of β Bootis (G8 III) from the composite spectrum produced better results than subtracting the spectrum of 24 Ursae Majoris (G2 IV), which implies that our best-fit types may be slightly too early for the G component and too late for the A component.

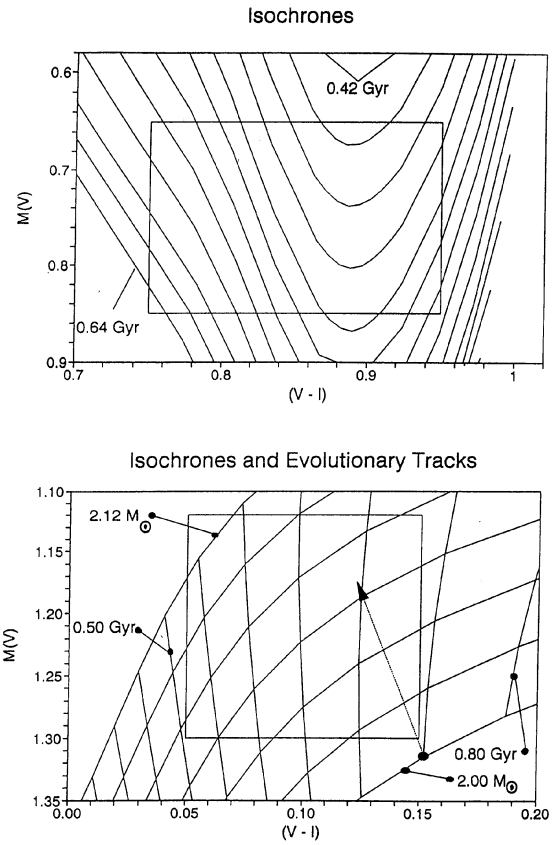


FIG. 3. (a) Isochrones at 0.02 Gyr intervals for the G component (primary). The outline shows the ±1σ error box for the derived $(V-I_C)$ and M_V. Evolutionary tracks are not shown, since they are nearly parallel to the isochrones in this part of the color–magnitude diagram. Ages of 0.43 and 0.65 Gyr correspond to $\mathcal{M}_G=2.75$ and $2.37\,\mathcal{M}_\odot$, respectively. (b) Isochrones at 0.05 Gyr intervals and evolutionary tracks at 0.02 $\mathcal{M}_\odot$ intervals for the A component (secondary) of α Equulei. The outline shows the ±1σ error box for the derived $(V-I_C)$ and M_V. The arrow indicates the direction of the shift of the curves if the metallicity Z is reduced; its length is half the shift due to a reduction in Z from 0.0169 to 0.0100.

6.3 Comparison with Evolutionary Models

Measurements of the masses, colors, and absolute magnitudes of two stars known to be of the same age and metallicity give us a test of models of stellar evolution, or conversely, the stellar evolutionary models can be used to check the derived quantities. With an appropriate choice of component masses, we can find a metallicity and an age that reproduce the observed colors and magnitude differences using an evolutionary model. The component masses needed for this model to reproduce the observed colors and magnitude differences are in good agreement with the mass derived from the orbital fits combined with the spectroscopic results.

We used the evolutionary models of VandenBerg (1985) to find the colors and magnitudes of the two com-

© American Astronomical Society • Provided by the NASA Astrophysics Data System

1992AJ....104..241A

ponents for various ages, masses, and metallicities. These models give M_{bol}, M_V, $(B-V)$, and $(V-I_C)$ as functions of mass and age for metallicities $0.0017 \leqslant Z \leqslant 0.0169$ $(=Z_\odot)$; I_C is on the Cousins system. The modifications to M_V and the $(B-V)$ colors given by VandenBerg and by Twarog & Anthony-Twarog (1989) were adopted: we subtracted 0m2 from VandenBerg's M_V, so our fits to the evolutionary model correspond to solar values of helium abundance Y and metallicity Z; we also added $\Delta=0.125(B-V)-0^m03$ to $(B-V)$ for $(B-V)\geqslant 0^m4$, which gives $(B-V)_\odot=0^m65$ for the model with solar age and metallicity.

Upon comparing the magnitudes and colors of the components of α Equulei to the corrected model magnitudes and colors, we found that only models with $Z=Z_\odot$ are consistent with the data; for lower Z, the G star has evolved up the giant branch by the time the A star attains the observed M_V, $(V-I_C)$, and $(B-V)$. We then tried to find pairs of stars with $Z=Z_\odot$ and the same age that matched the observed M_V and $(V-I_C)$. [This color was used because it is better determined by our data than is $(B-V)$; however, the results using $(B-V)$ are nearly the same.] Figure 3(a), which displays isochrones for the G component, and Fig. 3(b), which displays isochrones and evolutionary tracks for the A component, show the ranges of age and mass that fit the observed colors and magnitudes.

Using Figs. 3(a) and 3(b) together, one can see that a pair of model stars with the observed colors and magnitudes does exist. The $\pm 1\sigma$ uncertainties of the observed color and magnitude for the G component [Fig. 3(a)], correspond to a range in age from 0.43 Gyr, with $\mathcal{M}_G=2.75\,\mathcal{M}_\odot$, to 0.65 Gyr, with $\mathcal{M}_G=2.37\,\mathcal{M}_\odot$. (Note that the mass is nearly constant along an isochrone in this part of the color–magnitude diagram, since stars are quickly passing through on their way to the red giant branch.) The 1σ upper limit for $\mathcal{M}_G$ from our work is $2.42\,\mathcal{M}_\odot$. The color and absolute magnitude for the A star further restrict the age of the system to be greater than 0.5 Gyr [Fig. 3(b)]. Within these age constraints, the masses $\mathcal{M}_A$ that are within the 1σ errors of the derived color and magnitude lie between 2.03 and $2.13\,\mathcal{M}_\odot$. The 1σ upper limit for $\mathcal{M}_A$ from our work is $2.07\,\mathcal{M}_\odot$.

We consider the agreement between the measured masses and the masses estimated from the evolutionary models to be satisfactory, given the uncertainties in the models. The discussion by VandenBerg (1985) suggests that the model M_V values may be uncertain at the $\pm 0^m1$–0^m2 level. Making both evolutionary model stars brighter—i.e., moving the contours in Figs. 3(a) and 3(b) upward—by 0m2 would bring them into closer agreement with the orbital mass determinations and increase the range of acceptable ages for the system to 0.55–0.75 Gyr; this corresponds to removing the modification to M_V mentioned above. Making the models fainter by 0m2 would restrict the age to a narrow range around 0.55 Gyr and, more significantly, imply masses that are 1.5–2σ greater than the orbitally determined masses.

7. SUMMARY

We have measured the apparent orbit of the double-lined spectroscopic binary α Equulei with the Mark III Optical Interferometer. We combined these results with the spectroscopic results of Rosvick & Scarfe (1991) to obtain estimates of the masses of the components, their absolute magnitudes, and the distance to the system. We also determined the magnitude differences between the components at four wavelengths from the Mark III data. We combined these magnitude differences with the colors reported by Stickland (1976) to derive colors for the two components, and estimated their spectral types from these colors. Finally, we compared our derived colors and absolute magnitudes with the evolutionary models of VandenBerg (1985). We inferred the metallicity of the system from this comparison, but found that the masses determined by the orbital fitting, when used with the evolutionary models, gave colors and magnitudes somewhat in disagreement with the observed colors and magnitudes. With the current state of knowledge for α Equulei, the greatest need is for further spectroscopic observations, with the goals of improving the precision of the velocity curves and of measuring the metallicity of the system.

The number of spectroscopic binary systems for which orbits can be determined with the Mark III is between 10 and 30. Further results will add substantially to the list of well-determined stellar masses.

We thank Lu Rarogiewicz for his able assistance in operating the Mark III interferometer, and the anonymous referee for pointing out to us the difference between the spectroscopic and visual conventions for ω, and for suggesting several other improvements.

APPENDIX: MODEL FITTED TO VISIBILITY DATA

The model visibilities were calculated by integrating the monochromatic complex visibility of each binary component over the filter bandpass, and then summing the component visibilities weighted by the relative fluxes of the components. At each wavelength, the components were assumed to be uniform disks, but with different disk diameters for different wavelengths, to simulate the effect of limb darkening. The calibration constants C_λ were also included to reflect calibration errors.

In particular, the complex visibility of a single component j observed at wavelength band k of width $\Delta\nu_k$ is given by

$$V_{jk}=\frac{A_{jk}}{\Delta\nu_k}\int_{\nu_{0,k}-\Delta\nu_k/2}^{\nu_{0,k}+\Delta\nu_k/2} d\nu\,\frac{2J_1[\pi D_{jk}B(\nu)]}{\pi D_{jk}B(\nu)} \times\exp\left[2\pi\beta_j\left(\frac{\nu}{\nu_{0k}}\right)(u_{0k}\sin\alpha_j+v_{0k}\cos\alpha_j)\right]. \quad \text{(A1)}$$

Here,

$$A_{jk}=C_k\frac{10^{-0.4\Delta m_{jk}}}{1+\Sigma_{l=2}^{N}10^{-0.4\Delta m_{lk}}} \quad \text{(A2)}$$

© American Astronomical Society • Provided by the NASA Astrophysics Data System

1992AJ....104..241A

is the amplitude factor, in which C_k is the calibration constant at λ_k, N is the number of components, and Δm_{jk} is the magnitude difference at λ_k between component j and component 1. (The G component, which is brighter at λ800 nm, was designated as component 1.) Within the integral, $J_1(x)$ is the Bessel function of the first kind and first order, and α_j and β_j are the position angle and angular distance with respect to the phase center. The diameter D_{jk} at wavelength k is given by

$$D_{jk}=D_{j1}R_{jk}, \tag{A3}$$

where the diameter ratio R_{jk} is described by

$$R_{jk}=D_{jk}/D_{j1}. \tag{A4}$$

The length $B(\nu)$ of the projected baseline in the (u, v) plane is given by

$$B(\nu)=[u^2(\nu_0)+v^2(\nu_0)]^{1/2}(\nu/\nu_0), \tag{A5}$$

where ν_0 is the center wavelength of the filter.

In calculating the visibility of the binary, we assumed that the G component is at the phase center ($\beta=0$), since it contributes $\sim$75% of the flux at the fringe-tracking wavelength. Since neither star is actually at the phase center, the contributions of the two components to the visibility will be slightly in error. In the case of α Equulei, the effect at λ800 nm is that we overestimate the contribution from the G component by $\sim$0.04% and underestimate the contribution from the A component by $\sim$0.3%. At λ500 nm, the errors are 0.3% for the G component and 1.8% for the A component.

In Eq. (A1), we assume a square filter bandpass. The real bandpass due to the interference filters is not square; however, we estimate that the resulting error in V^2 is less than 0.2%, 0.8%, 1%, and 1.7% at 800, 550, 500, and 450 nm, respectively.

REFERENCES

Allen, C. W. 1976, Astrophysical Quantities, third edition (Athlone Press, London)
Batten, A. H., Fletcher, J. M., & MacCarthy, D. G. 1989, Publ. Dom. Astrophys. Obs., 17, 1
Bessel, M. S. 1976, PASP, 88, 557
Bessel, M. S. 1979, PASP, 91, 589
Bevington, P. R. 1969, Data Reduction and Error Analysis for the Physical Sciences (McGraw-Hill, New York)
Bonneau, D., Blazit, A., Foy, R., & Labeyrie, A. 1980, A&AS, 42, 185
Campbell, W. W. 1902, Lick Obs. Bull., 1, 158
Cannon, A. J., & Pickering, E. C. 1924, The Henry Draper Catalog, Harvard Ann., Vols. 91–99
Cousins, A. W. J. 1976a, MRAS, 81, 25
Cousins, A. W. J. 1976b, MNSAf, 35, 70
Cousins, A. W. J. 1978, MNSAf, 37, 8
Deutsch, A. J. 1954, PASP, 66, 58
Green, R. M. 1985, Spherical Astronomy (Cambridge University Press, Cambridge)
Hartkopf, W. I., & McAlister, H. A. 1984, PASP, 96, 105
Herbison-Evans, D., Hanbury Brown, R., Davis, J., & Allen, L. R. 1971, MNRAS, 151, 161
Hoffleit, D. , & Jaschek, C. 1982, The Bright Star Catalogue (Yale University Observatory, New Haven)
Johnson, H. L. 1966, ARA&A, 4, 193
Levato, H. 1975, A&AS, 19, 91
Maury, A. J., & Pickering, E. C. 1897, Harvard Ann., 28, 100, note 153
McAlister, H. A. 1978, PASP, 90, 288
Merrill, P. W. 1922, ApJ, 56, 40
Mozurkewich, D., *et al.* 1991, AJ, 101, 2207
Pédoussant, A., Carquillat, J. M., Ginestet, N., & Vigneau, J. 1988, A&AS, 75, 441
Pike, C. D. 1978, MNRAS, 184, 265
Popper, D. M. 1980, ARA&A, 18, 115
Press, W. H., Flannery, B. P., Teukolsky, S. A., & Vetterling, W. T. 1986, Numerical Recipes (Cambridge University Press, Cambridge)
Rosvick, J. M., & Scarfe, C. D. 1991, MNRAS, 252, 68
Shao, M., *et al.* 1988, A&A, 193, 357
Stickland, D. J. 1976, MNRAS, 175, 473
Stickland, D. J. 1988, in A Decade of UV Astronomy with the IUE Satellite (ESA SP-281), Vol. 2, p. 27
VandenBerg, D. A. 1985, ApJS, 58, 711
Vansina, F., & de Grève, J. P. 1982, Ap&SS, 87, 377
Vivekanand, M. 1990, AJ, 100, 2047

© American Astronomical Society • Provided by the NASA Astrophysics Data System